

# Bifurcation phenomena in Taylor–Couette flow in a very short annulus

By G. PFISTER,<sup>†</sup> H. SCHMIDT,<sup>†</sup> K. A. CLIFFE<sup>‡</sup>  
AND T. MULLIN<sup>§</sup>

<sup>†</sup>Institute of Applied Physics, University of Kiel, W. Germany

<sup>‡</sup>Theoretical Physics Division, AERE Harwell, Oxford OX1 0RA, UK

<sup>§</sup>Clarendon Laboratory, University of Oxford, Parks Road, Oxford OX1 3PU, UK

(Received 17 November 1986 and in revised form 4 November 1987)

We present the results of an experimental and numerical investigation into Taylor–Couette flow with gap-length to width ratios ( $\Gamma = l/d$ ) ranging from 0.3 to 1.4. Laser-Doppler-velocimetry is used to obtain quantitative information on the bifurcation set experimentally, and novel flow phenomena are uncovered. These results are compared with those obtained using numerical bifurcation techniques applied to a finite-element discretization of the Navier–Stokes equations. In general, the agreement is good and most of the observations are satisfactorily explained.

---

## 1. Introduction

The importance of end effects in selecting the steady cellular states of Taylor–Couette flow was recognized by Benjamin (1978*a, b*). He used Leray–Schauder degree theory to study the general properties of bifurcations among steady solutions of the Navier–Stokes equations. The degree arguments had previously been used by Velte (1964, 1966) to show the existence of solutions for cellular motion in Taylor’s (1923) infinite-cylinder model. Benjamin demonstrated the requirement that a minimum of nine solution branches is necessary to explain the exchange of stability between adjacent steady solutions. Thus, in any experiment where the cylinders are moderately long, the number of solutions is very large (Benjamin & Mullin 1982), so that a rigorous study of the nature of the bifurcations is difficult in practice. Thus the studies of finite-length effects have so far been concentrated on shorter cylinders where well controlled experiments are less difficult to perform because the set of possible solutions is limited.

The hysteresis phenomena associated with the exchange of stability between adjacent modes was demonstrated experimentally by Benjamin (1978*a, b*) and later extended to other modes by Mullin (1982) and Mullin, Pfister & Lorenzen (1982). A model to explain the hysteretic events was proposed by Schaeffer (1980) who used a homotopy parameter,  $\tau$ , to form a connection between the infinite-cylinder model ( $\tau = 0$ ) and the finite geometry ( $\tau = 1$ ) of the experiment. The model has been worked out in detail for a specific case by Hall (1982). The experimental and theoretical work was later confirmed to a large extent in the numerical work of Cliffe (1984) who also uncovered new aspects of the problem that are related to the reflection symmetry about the midplane.

A necessary consequence of both Benjamin’s and Schaeffer’s work is the existence of other stable, steady solution branches which are generally disconnected from those

found at small Reynolds numbers  $R$ . These are the anomalous modes and are so called because they have a direction of rotation of one or both end cells such that there is outward flow along either or both endwalls. This is contrary to the long-held belief that as the centrifugal force falls off towards the ends of the cylinders then there must be inward-directed flow at the stationary endwalls. An extended study of the properties of the anomalous modes was given by Benjamin & Mullin (1981) and many of the findings were later confirmed by Cliffe & Mullin (1985) and Bolstad & Keller (1987).

The work of Benjamin & Mullin also demonstrated the existence of a single-cell mode at very small values of the non-dimensionalized length, the aspect ratio  $\Gamma = l/d$ , where  $l$  is the length of the annulus and  $d = r_2 - r_1$ . Casual observation of the single-cell state was also made in an independent study by Thomas (1979). Benjamin & Mullin used Schaeffer's model to interpret their experimental results and all of the salient features have subsequently been confirmed in both numerical and experimental work by Cliffe (1983), Schmidt (1983), Lücke *et al.* (1984) and Aitta, Ahlers & Cannell (1985).

At very small values of the aspect ratio the single-cell states remain connected to the two-cell primary flow which develops smoothly from  $R = 0$ . The process whereby disconnection occurs is illustrated in figure 1. In figure 1(a) we see that the primary two-cell state loses stability to a pair of single-cell states at  $R_{c_1}$  through a supercritical bifurcation. It regains stability at a higher value of  $R$  by shedding a pair of unstable branches at  $R_{c_2}$ . Of course, in any real experiment, imperfections would disconnect these bifurcations so that one would observe the smooth development of a single cell with a preferred direction of rotation. Nevertheless, both states are observable in the experiment although one is only reached by a trick such as a sudden start of the apparatus to a value of  $R$  above  $R_{c_2}$ . We consider the imperfection-free case in figure 1 in order to simplify the explanation. The supercritical bifurcation has been studied by Lücke *et al.* and detailed comparison between experiment and numerical results has been given.

As the aspect ratio is increased the bifurcation at  $R_{c_1}$  develops quartic contact, becoming subcritical as shown in figure 1(b). Now there is hysteresis in the development of the single-cell states and the interaction with the two-cell state above  $R_{c_2}$  is increased. The change from supercritical to subcritical bifurcation has been studied in detail experimentally by Aitta *et al.* (1985).

Further increase in  $\Gamma$  leads to the disconnection of the single-cell states, as shown in figure 1(c), so that they now become true secondary modes. The complete picture described above was observed experimentally by Benjamin & Mullin (1981) and Schmidt (1983), and confirmed numerically by Cliffe (1983). It is interesting to note that the single-cell state is apparently the only anomalous mode that remains connected in this way. The other odd-numbered modes are disconnected in a similar manner but do so as the Schaeffer homotopy parameter varies from  $\tau = 0$  (the periodic model case) to  $\tau = 1$  (the physical situation). Thus all other odd-cell modes are disconnected pairs of states and do not interact with the primary states.

The aim of the present investigation was first to study the complete disconnection procedure at a smaller value of the radius ratio  $\eta = r_1/r_2$ . This involved an experimental study at  $\eta = 0.5$  and complementary numerical work using modern numerical bifurcation techniques. The numerical methods have previously been described in detail by Cliffe & Spence (1985) and consist of continuation methods applied to a finite-element discretization of the Navier-Stokes equations. A brief outline of these methods is given in §3.

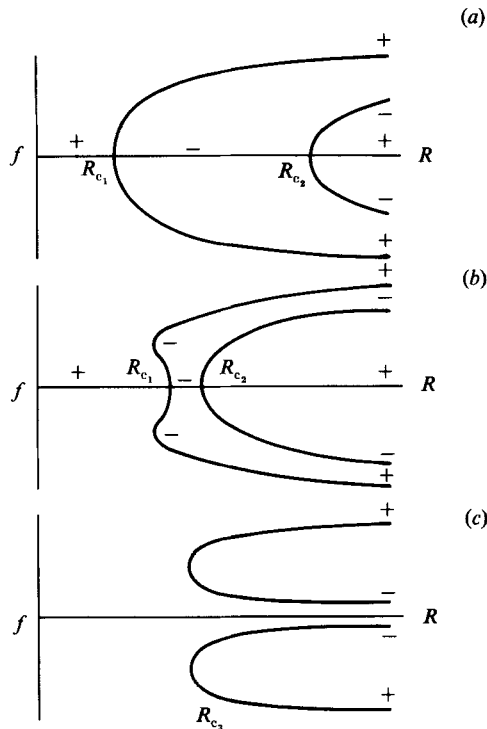


FIGURE 1. Bifurcation diagrams showing the interaction of the two-cell and one-cell flows. A linear functional (such as the axial velocity at the midplane) distinguishing the asymmetric flows is plotted against  $R$ . Branches with a negative sign denote unstable solutions.  $R_{c_1}$  denotes the critical Reynolds number for the supercritical and the subcritical bifurcations which give rise to the single-cell flows.  $R_{c_2}$  marks the bifurcation point for the two-cell secondary mode and  $R_{c_3}$  is the lower limit of stability of the one-cell modes. The aspect ratio increases from (a) to (b) to (c).

The experiments consisted of using laser-Doppler velocimetry (LDV) to obtain high-quality data on the nature of the bifurcations involved by measuring the changes in the stable branches as the aspect ratio is varied. In addition, an attempt was made to obtain indirect measurements of the unstable branches which helps to clarify the complete solution map and can be compared with those computed numerically. At very small values of the aspect ratio, a new and unsuspected solution branch was first found experimentally and subsequently identified numerically indicating that the original model is in some sense incomplete. Further, the discovery of the new steady flows led directly to the uncovering of a period-doubling route to chaos (Pfister 1985). It is thought that this is possible because of the limited number of spatial modes available to the flow at such small aspect ratios. Finally, some conclusions are drawn about the present findings and suggestions are made for future work since there are indications that, even in this very restricted range of parameter space, our knowledge of the solution set may yet be incomplete.

## 2. Apparatus and measuring techniques

The inner cylinder of our Taylor–Couette apparatus was machined from stainless steel and had a radius of  $r_1 = 11.5$  mm, while the outer cylinder was machined from Perspex and its radius was  $r_2 = 23.0$  mm. Thus the radius ratio was  $\eta = r_1/r_2 = 0.5$ .

the so-called wide-gap case. The accuracy of the radii was better than 0.01 mm over the entire length. The flow regime of interest was contained between stationary bottom and top plates. The gap length could be varied continuously by moving the metal collar which provided the top surface of the flow domain. The metal collar was held by three stainless-steel rods. This construction allowed a variable tilting angle between the top plate and the plane perpendicular to the rotation axis of about  $0.1^\circ$ . The majority of the experiments were carried out with a zero tilt angle. However, the effect of variation of the tilt angle upon the bifurcations was investigated. This point will be discussed later in the presentation of the results.

The corners of the gap were manufactured to better than 0.02 mm and it was found experimentally that their effects did not penetrate far into the fluid. The fluid confined in the gap was silicone oil with a kinematic viscosity  $\nu = 0.35 \text{ cm}^2 \text{ s}^{-1}$  at  $25^\circ \text{C}$  with an uncertainty in the absolute value of about 1%. The dynamical parameter is the Reynolds number defined as  $R = \Omega d r_1 / \nu$ , where  $\Omega$  is the angular frequency of the rotation for the inner cylinder, and  $d = r_2 - r_1$  is the width of the annular gap. The temperature of the fluid was held constant to within 0.01 K by circulating thermostatically controlled silicone oil through a surrounding square box. The error in the orientation of the LDV fringe system, caused by slight refractive index mismatch, was minimized by rotating the outer box through a small angle. The magnitude of the error was determined by comparing measurements of the radial velocity made with the inner cylinder rotating in opposite directions. The angle of rotation of the box was chosen so that this source of error was negligible.

A phase-locked-loop circuit controlled the speed of the inner cylinder to better than one part in  $10^{-4}$  in the short term and better than one part in  $10^{-6}$  on the long-term average. Thus the accuracy of the absolute value of the Reynolds number was about 1% and for relative changes better than  $10^{-5}$ . The local velocity was measured by a real-fringe Doppler anemometer using a phase-locked-loop (PLL) tracker for analogue recording of the velocity (Hille 1984). Two Bragg cells were used to determine the velocity direction by applying a bias to the signal. The Bragg shift of both cells was 40 and 40.1 MHz, transferring the zero velocity to 100 kHz. The tracker operated in the range of 15 to 200 kHz giving a suitable measurement range for the velocity. The working fluid had to be seeded to obtain proper signal quality. For this purpose the silicone oil was seeded with Latex spheres of diameter  $2 \mu\text{m}$ , which was suited to the fringe spacing of about  $3 \mu\text{m}$  in this experimental set-up. Since the Latex spheres could be obtained only in an aqueous solution, they had first to be dried and then suspended in the silicone oil by the use of an ultrasonic generator.

Further signal processing (Pfister *et al.* 1983) yielded the velocity correlation function and the velocity power spectrum directly. By this means we could accurately determine whether the flow was stationary or showed time-dependent behaviour. With a motor-driven lift for the  $z$ -direction and a precision  $x$ - $y$  table the measurement volume of the LDV system could be placed anywhere in the gap. Additionally the location of the lift could be recorded versus the analog output of the PLL tracker to obtain an axial velocity profile using either the radial or axial component of velocity. All the velocity-Reynolds-number diagrams were obtained by continuously recording the velocity as the Reynolds number was changed quasi-statically. Figure 7 shows the unfiltered data, all the other figures show filtered data with the LDV noise removed.

### 3. Numerical methods

In cylindrical polar coordinates  $(r^*, \theta, z^*)$  with the origin midway between the ends of the annular gap and velocity  $\mathbf{u}^* \equiv (u_r^*, u_\theta^*, u_z^*)$ , the equations for axisymmetric flow of a viscous, incompressible fluid are

$$\frac{\partial u_r}{\partial t} + R \left\{ u_r \frac{\partial u_r}{\partial r} + u_z \frac{\partial u_r}{\partial z} - \frac{u_\theta^2}{r + \beta} \right\} + \frac{\partial p}{\partial r} - \left\{ \frac{1}{r + \beta} \frac{\partial}{\partial r} (r + \beta) \frac{\partial u_r}{\partial r} + \frac{1}{\Gamma^2} \frac{\partial^2 u_r}{\partial z^2} - \frac{u_z}{(r + \beta)^2} \right\} = 0, \quad (1)$$

$$\frac{\partial u_\theta}{\partial t} + R \left\{ u_r \frac{\partial u_\theta}{\partial r} + u_z \frac{\partial u_\theta}{\partial z} + \frac{u_r u_\theta}{(r + \beta)} \right\} - \left\{ \frac{1}{r + \beta} \frac{\partial}{\partial r} (r + \beta) \frac{\partial u_\theta}{\partial r} + \frac{1}{\Gamma^2} \frac{\partial^2 u_\theta}{\partial z^2} - \frac{u_\theta}{(r + \beta)^2} \right\} = 0, \quad (2)$$

$$\frac{\partial u_z}{\partial t} + R \left\{ u_r \frac{\partial u_z}{\partial r} + u_z \frac{\partial u_z}{\partial z} \right\} + \frac{1}{\Gamma^2} \frac{\partial p}{\partial z} - \left\{ \frac{1}{(r + \beta)} \frac{\partial}{\partial r} (r + \beta) \frac{\partial u_z}{\partial r} + \frac{1}{\Gamma^2} \frac{\partial^2 u_z}{\partial z^2} \right\} = 0, \quad (3)$$

$$\frac{1}{(r + \beta)} \frac{\partial}{\partial r} (r + \beta) u_r + \frac{\partial u_z}{\partial z} = 0. \quad (4)$$

In the above equations  $r$ ,  $z$ ,  $\mathbf{u}$  and  $p$  are given by

$$r = \frac{r^*}{d} - \beta, \quad z = \frac{z^*}{l}, \quad \mathbf{u} = \frac{1}{r_1 \Omega} \left( u_r^*, u_\theta^*, \frac{u_z^*}{\Gamma} \right), \quad p = \frac{dp^*}{\mu r_1 \Omega},$$

and

$$t = t^* \Omega \frac{\eta}{R(1 - \eta)},$$

where  $d = r_2 - r_1$ ,  $\beta = r_1/d = \eta/(1 - \eta)$  and  $\eta = r_1/r_2$  is the radius ratio. The aspect ratio  $\Gamma = l/d$  and the Reynolds number  $R = \rho r_1 \Omega d / \mu$ , where  $\rho$  and  $\mu$  are the fluid density and viscosity respectively.

Equations (1)–(4) hold in the region  $D$  where

$$D = [(r, z) | 0 \leq r \leq 1, -0.5 \leq z \leq 0.5]. \quad (5)$$

The boundary conditions are such that  $u_r$  and  $u_z$  are zero on the entire boundary, and that  $u_\theta$  is zero on the outer cylinder ( $r = 1$ ) and 1 on the inner cylinder ( $r = 0$ ).  $u_\theta$  is also zero at the ends ( $z = \pm 0.5$ ) except near the inner cylinder where it increases smoothly to 1 over a small distance,  $\epsilon$ . In the experiment the corresponding value of  $\epsilon$  and the variation of  $u_\theta$  are unknown; however, we have found the numerical results to be insensitive to the value of  $\epsilon$  provided that it is sufficiently small.

The numerical treatment of (1)–(4) is based on the finite-element method combined with techniques from numerical bifurcation theory. The finite-element method is used to discretize the  $(r, z)$ -region  $D$ , and the  $t$ -variable is not discretized. This leads to a set of ordinary differential equations in  $t$ , the dependent variables being velocity and pressure degrees of freedom in the  $(r, z)$ -discretization. We may write these equations in the form

$$M \frac{\partial \mathbf{x}}{\partial t} + \mathbf{f}(\mathbf{x}, R, \Gamma) = 0. \quad (6)$$

Steady axisymmetric flow is governed by the equation

$$\mathbf{f}(\mathbf{x}, R, \Gamma) = 0. \quad (7)$$

Methods for treating (7) have previously been used to study the Taylor–Couette problem (Cliffe 1983; Cliffe & Mullin 1985; Cliffe 1984) and numerical details for

computing solution branches, paths of limit points, paths of symmetry-breaking bifurcation points and paths of Hopf bifurcation points may be found in Cliffe & Spence (1986) and Cliffe, Jepson & Spence (1986). The linear stability of a steady solution  $(\mathbf{x}_0, R_0, \Gamma_0)$  of (7) may be examined using the eigenvalue problem

$$\mathbf{f}_x \boldsymbol{\xi} = \sigma M \boldsymbol{\xi}. \quad (8)$$

If all eigenvalues  $\sigma$  have  $\text{Re } \sigma > 0$  then  $\mathbf{x}_0$  is linearly stable. If there is one eigenvalue with  $\text{Re } \sigma < 0$  then the flow is unstable and the time constant for the growth of the unstable mode is  $\tau^*$  s, where

$$\tau^* = \frac{R(1-\eta)}{\sigma \Omega \eta}. \quad (9)$$

The behaviour of a given eigenvalue along a solution branch can be determined by applying the standard continuation techniques of Keller (1977) to the system consisting of (7) and (8) together with a normalization condition on the eigenvector  $\boldsymbol{\xi}$ . In the eigenvalue calculation performed here, a starting point for the continuation procedure was taken to be a point on the path of symmetry-breaking bifurcation points where  $\sigma = 0$  and the eigenvector is available from the extended system for the bifurcation point.

The stability of symmetric flows near a symmetry-breaking bifurcation point can be studied by calculating the rate of change of the zero eigenvalue with Reynolds number,  $\partial\sigma/\partial R$ . If  $\boldsymbol{\xi}_0$  is the singular right eigenvector and  $\boldsymbol{\zeta}_0$  is the corresponding left eigenvector then we have

$$\frac{\partial\sigma}{\partial R} = \frac{\boldsymbol{\zeta}_0(\mathbf{f}_{xx}^0 \boldsymbol{\xi}_0 \mathbf{v}_R + \mathbf{f}_{xR} \boldsymbol{\xi}_0)}{\boldsymbol{\zeta}_0 M \boldsymbol{\xi}_0}, \quad (10)$$

where

$$\mathbf{f}_x^0 \mathbf{v}_R + \mathbf{f}_R^0 = 0 \quad (11)$$

and  $\mathbf{f}^0 \equiv \mathbf{f}(\mathbf{x}_0, R_0, \Gamma_0)$  etc, where  $(\mathbf{x}_0, R_0, \Gamma_0)$  is the symmetry-breaking bifurcation point.

The calculations of the symmetric flows and symmetry-breaking bifurcation points were performed using techniques to exploit the symmetry (Cliffe & Spence 1986) so that only half the domain  $D$  was discretized. Most of the calculations were done on a uniform mesh with 20 elements in the  $r$ -direction and 10 in the  $z$ -direction. The results were checked on a  $40 \times 20$  grid at several points and it was found that an overall accuracy of better than 1% was achieved. The asymmetric flows and limit points were calculated on the full domain using  $20 \times 20$  and  $40 \times 40$  meshes respectively. Finally, local refinement was used near the corners where the rotating inner cylinder meets the stationary ends (see Cliffe 1983).

#### 4. Results

The flows we consider in this paper are illustrated in figure 2. The figure shows computed streamline plots for the symmetric two-cell and the single-cell states for an aspect ratio  $\Gamma = 1$ , where i and o stand for the inner and outer cylinder and b and t the bottom and top plate respectively. A more detailed discussion of the flow pattern at this aspect ratio is given by Lücke *et al.* (1984). The two-cell flow is mirror symmetric relative to the midplane with the maximum outward flow velocity lying in this plane. The axial velocity component, in the midplane, of the symmetric two-cell state is zero for all Reynolds numbers.

For the single-cell there exist two equivalent modes each with a large main vortex and a small weak one near the top or bottom plate respectively. In contrast to the

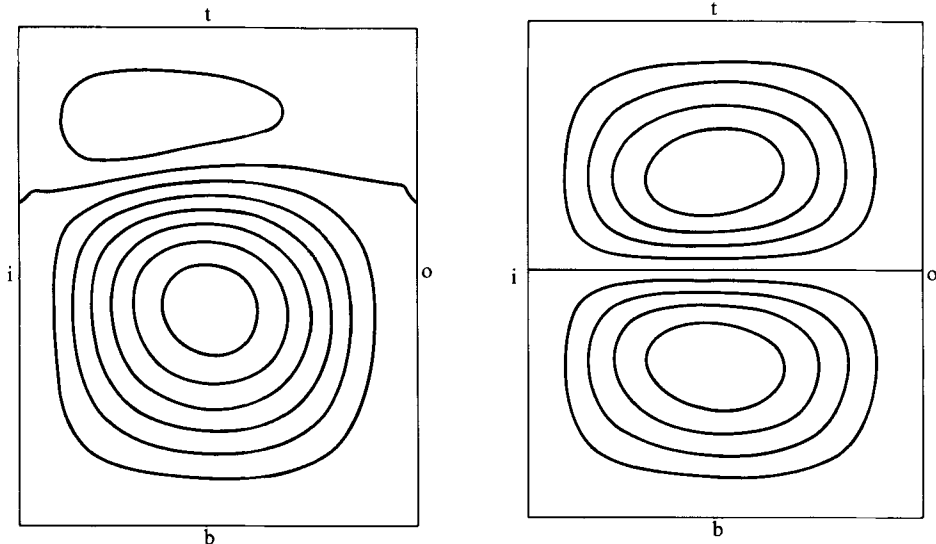


FIGURE 2. Computed streamlines for the two-cell and single-cell states for an aspect ratio  $\Gamma = 1.0$ : o and i indicate outer and inner cylinder and t and b the top and bottom plates. Note that there is always a small secondary vortex visible in one corner which is very much weaker than the main vortex. We refer to this flow as the single-cell state as this defines the origins of the flow more clearly.

symmetric mode, the axial velocity component is non-zero in the midplane for all radii. With appropriate adjustment it is therefore possible to characterize the actual flow mode by a measurement of a single local velocity component. However, in practice it is more convenient to measure the local radial velocity component. Unfortunately, it is not possible to distinguish between the asymmetric states using only the radial component. Therefore we have measured both the radial and axial component, mainly using the latter for identification of the flow mode.

Figure 3 shows the radial velocity component in the middle of the gap plotted against height, for the three possible modes. Profile  $s$  shows the symmetric state and profiles  $a_t$  and  $a_b$  the two asymmetric states respectively. Thus velocity measurements in the middle of the gap at the midplane may be used to obtain information about the type of flow present in the annulus and give a measure of the asymmetry in the flow. We used this as a linear functional which discriminates between the flow modes.

#### 4.1. Stable branches

The measurement techniques outlined in §2 were used to obtain the loci of critical points for the various bifurcations as a function of  $\Gamma$ . The results are shown in figure 4 where we have also plotted the numerically determined curves for comparison. We shall now discuss each portion of the stability diagram in detail.

The section of the curve labelled AB is the locus of the supercritical bifurcation points for the appearance of the single-cell state. The smallest value of aspect ratio obtainable was 0.34 which was a limitation imposed by the geometry of the laser beams used in the measuring system. The bifurcation is disconnected by the presence of imperfections in the apparatus and thus there is a smooth development of one of the single-cell flows. Nevertheless, a good estimate of the bifurcation point could be

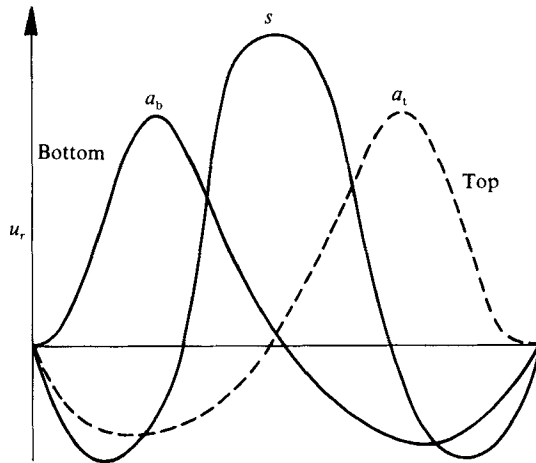


FIGURE 3. Experimental radial velocity component versus height for the flow modes shown in figure 2. The profiles are taken in the middle of the gap for an aspect ratio  $\Gamma = 1.264$  and  $R = 122.0$ . Profile  $s$  shows the symmetric flow mode whereas the profiles  $a_b$  and  $a_t$  show the two single-cell modes that are possible for these boundary conditions.

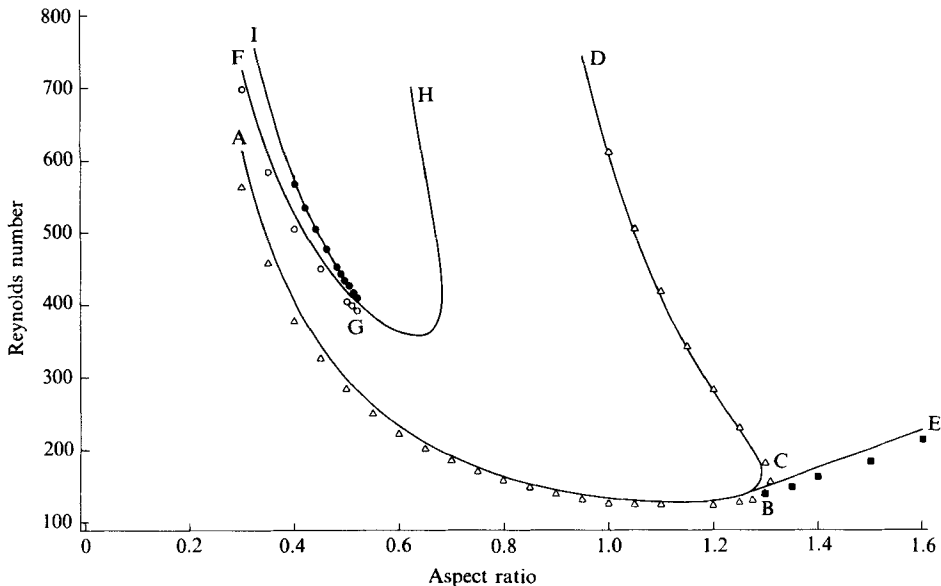


FIGURE 4. Experimental and numerically determined bifurcation set for the one-two-cell interaction. The solid lines are numerically determined, and the symbols mark the experimental data points: ABCD and  $\triangle$ , path of symmetry-breaking bifurcation points; BE and  $\blacksquare$ , path of limit points on the single-cell solution sheet; FGH and  $\circ$ , new path of symmetry-breaking bifurcation points; IG, path of axisymmetric Hopf bifurcation points;  $\bullet$ , experimentally observed transition to axisymmetric oscillations.

obtained from the sharp change in the slope of the radial velocity as a function of  $R$ , as may be seen in figure 5.

As the aspect ratio is increased towards B, in figure 4, there is a pronounced steepening in the measured-axial-velocity plots as shown in figure 6. This indicates the presence of a quartic point at B where the supercritical bifurcation changes

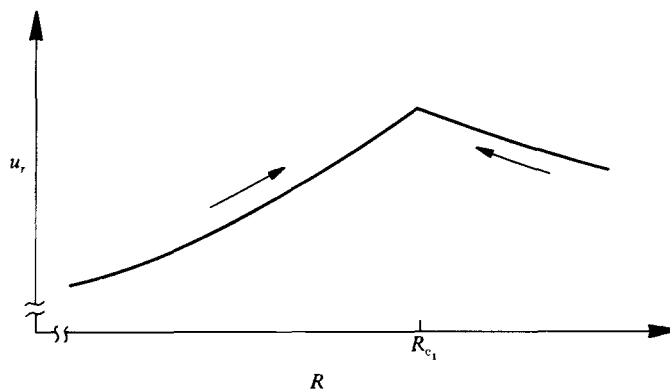


FIGURE 5. Experimental radial velocity component versus Reynolds number showing a supercritical bifurcation from a symmetric two-cell state to a single-cell state. The trace is the same for increasing and for decreasing Reynolds number. The kink in the curve indicates the critical point.

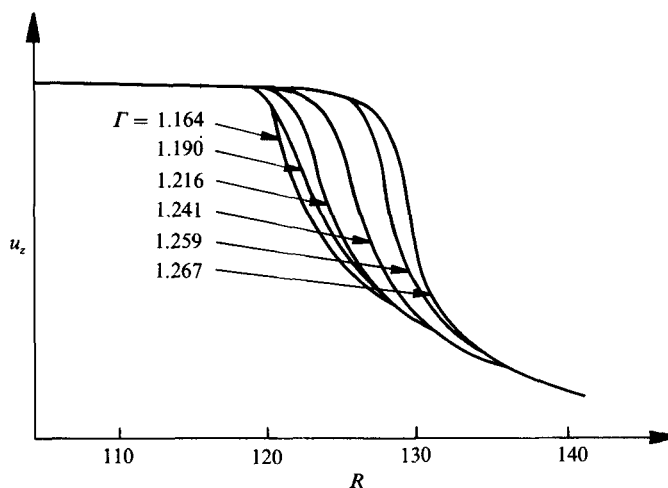


FIGURE 6. Experimental axial velocity component versus Reynolds number for aspect ratios near the point B in figure 4 showing the pronounced steepening as the quartic point is approached.

to a subcritical one with increasing  $\Gamma$ . In the very small aspect-ratio range  $\Gamma = 1.267$ – $1.304$  the flow exhibits subcritical behaviour with its associated hysteresis. The plots of measured vertical velocity against  $R$  for this region are shown in figure 7; we also show an enlarged  $(R, \Gamma)$ -plot in figure 8 to highlight the hysteresis. The hysteresis phenomenon is a delicate feature which requires very tight experimental control to assure repeatable measurements. However, the critical points are well defined and an accurate estimate of their values can be made in the experiment. The delicate nature of the events can perhaps account for the discrepancy between the numerical results and the experiments in this region as the hysteresis phenomena may be extremely sensitive to small imperfections in the apparatus.

The two-cell secondary branch may also be seen in figure 7. As  $\Gamma$  is increased from 1.267 to 1.304 the interaction between the two-cell primary and secondary states increases so that for  $\Gamma$  slightly greater than 1.304 there is a continuous connection of the two-cell state. The line CD in figure 4 shows the locus of symmetry-breaking bifurcation points for the two-cell secondary mode.

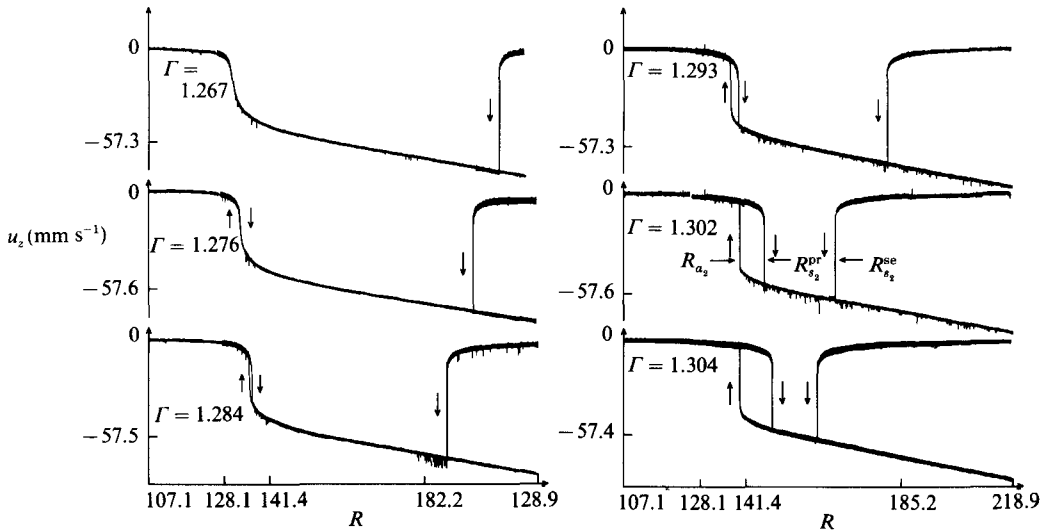


FIGURE 7. Plots of experimentally measured axial velocity component versus  $R$ , in the hysteresis region. The secondary two-cell state is also shown. The data in these diagrams has not been filtered in order to illustrate the noise level in the LDV system.

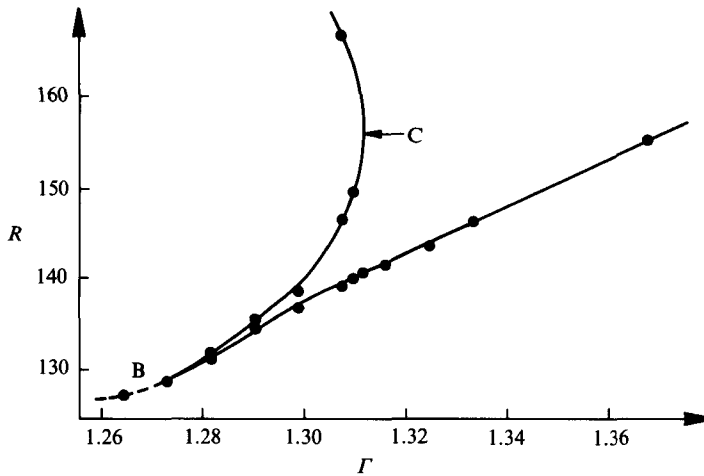


FIGURE 8. Enlargement of the hysteretic part of figure 5 (experiment only).

The single-cell modes thus become disconnected and are now true secondary modes as they cannot be reached by a smooth change in  $R$ . They may only be obtained by a jump to a value of  $R$  above the critical value. A typical experimental axial velocity versus  $R$  plot is shown in figure 9 where we have included measurements for both single-cell states to highlight the usefulness of measuring the vertical component of velocity. The locus of the lower limits of stability of the single-cell states as a function of  $\Gamma$  is labelled BE in figure 4.

All of the above results are in qualitative agreement with those obtained previously in the flow-visualization experiments of Benjamin & Mullin (1981). They covered the aspect-ratio range of 0.65 to 1.5 using apparatus with a radius ratio of 0.615. The results obtained here indicate an overall shift towards lower values of  $R$  for a reduction in radius ratio.

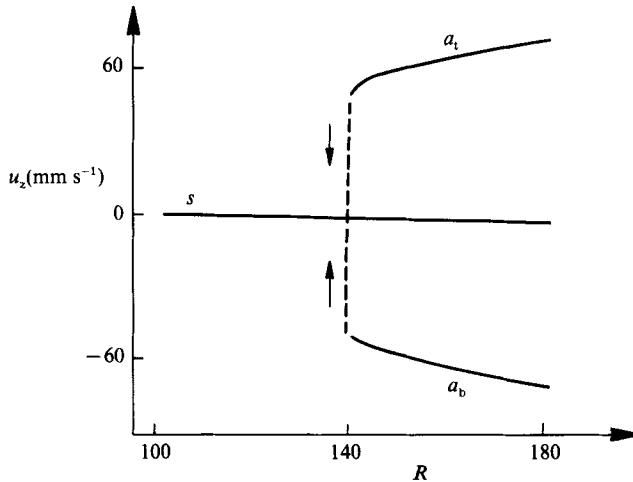


FIGURE 9. Plot of axial velocity component versus Reynolds number showing the collapse of the two single-cell modes to the symmetric primary mode. The slight difference in critical Reynolds numbers arises owing to small imperfections in the apparatus which destroy the perfect symmetry.

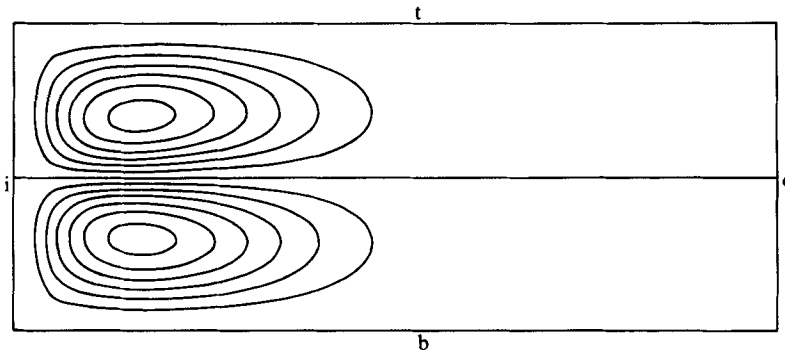


FIGURE 10. Computed streamlines for the new two-cell flow at aspect ratio 0.4 and Reynolds number 525: o and i indicate outer and inner cylinder and t and b the top and bottom plates.

It was anticipated that a period-doubling sequence could be found at these small values of aspect ratio where the number of spatial modes is strictly limited. During the search for this feature a new steady flow was uncovered. This had the appearance of a two-cell symmetric flow with the cells compressed towards the inner cylinder. It was not possible to obtain good quality photographs of this flow; however, the observations corresponded closely to the numerically computed streamline patterns, an example of which is shown in figure 10.

The new flow was computed numerically by continuation in the Reynolds number along the primary, symmetric two-cell branch beyond the first symmetry-breaking bifurcation at an aspect ratio of 0.4. The determinant of the antisymmetric Jacobian matrix was monitored along the branch and a change in sign was detected indicating a symmetry-breaking bifurcation. The path of these symmetry-breaking bifurcations, FGH in figure 4, was computed using the Werner–Spence extended system (Cliffe & Spence 1985) and continuation in the aspect ratio.

The two-cell flow is stable outside the region ABCD and loses stability as this line is crossed. Since the line ABCD is a path of singular points with one-dimensional null

space it follows that there is only one eigenvalue with negative real part (i.e. which is unstable) in the region between ABCD and FGH. The value of  $\partial\sigma/\partial R$ , where  $\sigma$  is the zero eigenvalue at the bifurcation point, was computed (from (10)) along the path FGH. It was found that  $\partial\sigma/\partial R > 0$  along FG and  $\partial\sigma/\partial R < 0$  along GH. Thus the eigenvalue that is singular along FG is negative below FG and positive just above it. Since there is only one negative eigenvalue in the region bounded by FGH and ABCD, it follows that this eigenvalue passes through zero as FG is crossed and that the two-cell flow is stable just above FG. However, the eigenvalue that is singular along GH is positive below GH and negative above it, so that as GH is crossed the number of negative eigenvalues increases from 1 to 2.

If we now vary the aspect ratio and keep the Reynolds number fixed at a value just above that corresponding to G, we have a solution with two negative eigenvalues, to the right of G, changing continuously into one with no negative eigenvalues, to the left of G, without crossing any simple bifurcation points. This situation is resolved by the existence of an axisymmetric Hopf bifurcation: that is the two negative eigenvalues coalesce to form a complex-conjugate pair with negative real part which then cross the imaginary axis (at the Hopf bifurcation point) and coalesce to give two positive real eigenvalues. The line GI of axisymmetric Hopf bifurcation points was computed numerically using the appropriate extended system and continuation techniques.

The new two-cell flow was found experimentally by switching to a value of  $R$  just above FG from the one below AB. Once the flow had settled down,  $R$  was gradually reduced and the critical value for collapse into the single-cell state was estimated in the usual way. The agreement between the experimental points and the numerically determined curve is reasonable. The new two-cell flow was not observed for aspect ratios greater than that corresponding to point G.

When  $R$  was increased the two-cell flow lost stability to an axisymmetric oscillation. The motion was observed to be in phase around the cylindrical gap using a split laser-Doppler system. It can be seen from figure 4 that the agreement between the computed path of Hopf bifurcations, GI, and the experimentally determined points for the onset of the oscillation is good. In addition we have measured the frequency near the onset of the oscillation and the comparison with the numerically computed values is given in figure 11. The agreement is satisfactory although there appears to be some small systematic discrepancy as the point G is approached.

An unresolved feature of the results is the sensitivity of the bifurcation giving rise to the new two-cell flow to small imperfections. It was observed in the experiments that a small tilt of the upper boundary (about  $0.1^\circ$ ) could produce two slightly asymmetric states from the single symmetric state. This seems to indicate that a small imposed imperfection changed the supercritical bifurcation into a subcritical one. It could be argued that the introduction of a small three-dimensional effect into the experiment renders the comparison with the axisymmetric numerical model meaningless. However, the amount of tilting was so small that it was close to the accuracy limits of the present apparatus. This perhaps indicates that the bifurcation is strongly imperfection sensitive and may be amenable to a linear stability analysis about the numerical solution. It is perhaps worth mentioning that we have not found this type of sensitivity in any of our previous studies of bifurcation phenomena and a further investigation is planned.

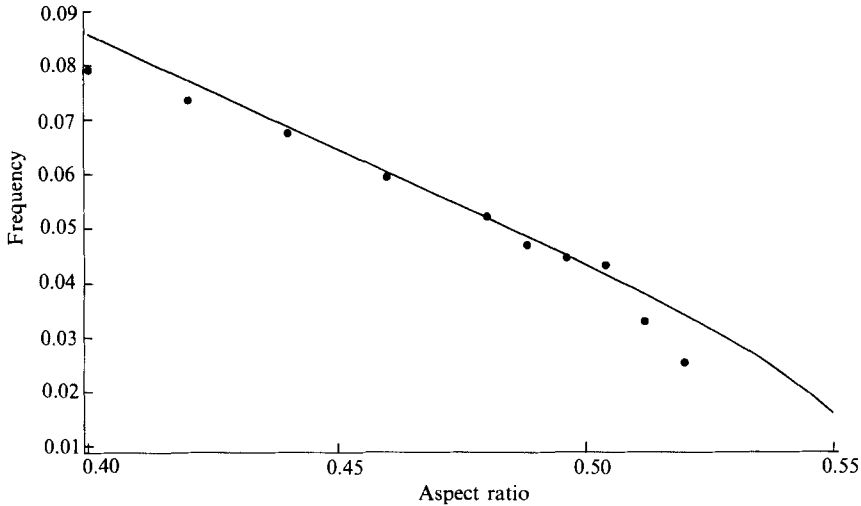


FIGURE 11. Comparison between calculations (—) and measurements (●) of the non-dimensionalized frequency for the axisymmetric oscillation of the new two-cell flow as the aspect ratio is varied. The frequencies are non-dimensionalized with respect to the inner-cylinder frequency.

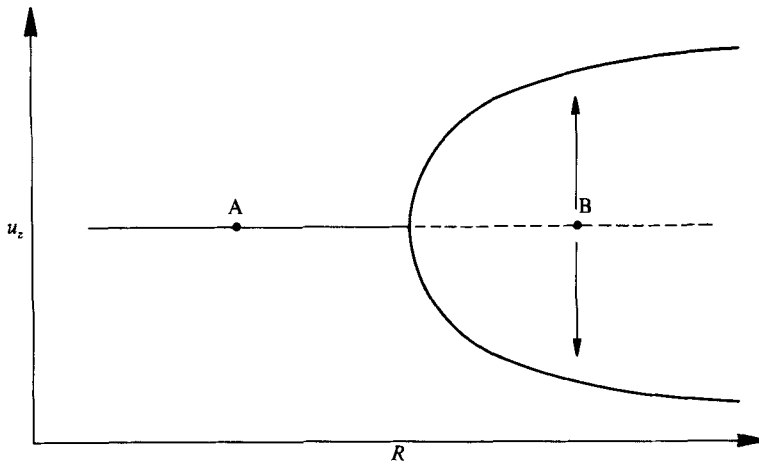


FIGURE 12. An illustration of the experimental technique used to examine the unstable flows.

#### 4.2. Unstable branches

The unstable flows are of course respectable solutions of the complete mathematical problem. However, they are unobservable directly in any experiment since any small perturbation will grow exponentially and the flow will rapidly collapse to a nearby stable one. In an attempt to elucidate the complete solution set further we have devised an experimental method for indicating the behaviour of the flow near conjectured unstable branches.

The experimental method consists of starting with a steady stable flow and switching the Reynolds numbers suddenly to a region where we expect an unstable branch to exist. As an illustrative example of the technique we refer to figure 12. Starting from point A to the left of the bifurcation point,  $R$  is suddenly increased to point B on the unstable branch. The change in  $R$  takes place in 0.01 s whereas it takes

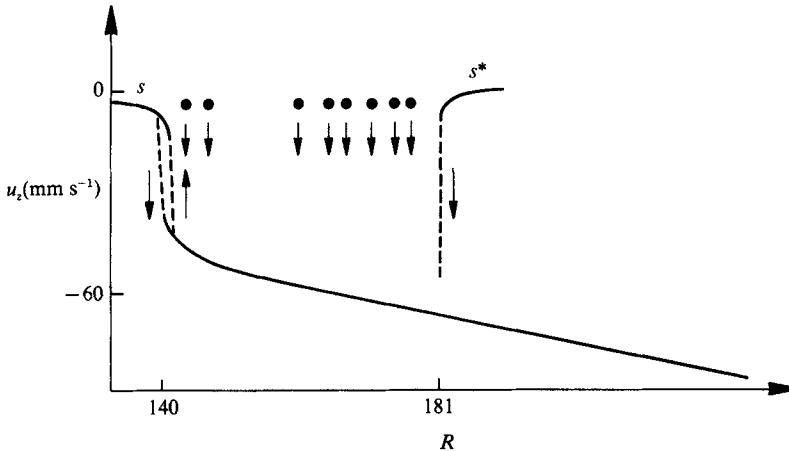


FIGURE 13. Measured bifurcation diagram showing a plot of axial velocity versus  $R$  for  $\Gamma = 1.3$ . The circles indicate the estimates of the unstable part of the two-cell branch.

$\sim 0.2$  s for the flow to collapse to either of the stable branches in a well-defined relaxation process. Close to bifurcation points, this time can be as long as 1 min. The boundary of attraction is located when there is an equal likelihood of collapse in either direction towards nearby stable states. In addition, the relaxation time reaches a maximum at these points.

This technique was used to investigate the case when  $\Gamma = 1.3$ , where there is hysteresis in the development of the single-cell state. In figure 13 we show a plot of the axial velocity component  $u_z$  for the symmetric two-cell states  $s$  and  $s^*$  and one stable branch of the single-cell state. After locating the boundary of attraction of both single-cell states by the method outlined above, we made measurements of the growth rate from these points. For this purpose the starting points on  $s$  were chosen to be very close to the bifurcation point for the onset of the single-cell state. At these points imperfections in the apparatus naturally provide a slightly asymmetric starting state so that the flow always collapses towards a preferred single-cell state as shown in figure 13.

The change of  $u_z$  with time could then be recorded for the relaxation process towards the stable states. Examples of these measurements are shown in figure 14 where the numbers on the various traces indicate the final Reynolds numbers. We fitted the initial slopes of the traces with an exponential, i.e.  $\exp(t/\tau)$ , and thus estimated the time constants which are shown in figure 15(a). Figure 15(b) shows the time constants of the same process obtained from numerical calculations by the method outlined in §3. The qualitative form of the two sets of results are strikingly similar. We were unable to make a direct quantitative comparison because of the discrepancy between the experimental and numerical results for the critical values for the onset of the single-cell state. As mentioned above, we believe that the hysteresis region is extremely sensitive to imperfections, which may help to explain these differences. However, we chose to measure the relaxation times in this region owing to the closeness of both bifurcation points.

Encouraged by this we have extended the experimental method to the boundary of attraction which separates the stable two-cell state  $s^*$  and the single-cell states. In this case the starting points were chosen on the branches  $a_c$  and  $a_b$  (see figures 3 and 16). By applying the method described above we could obtain a good estimate for the

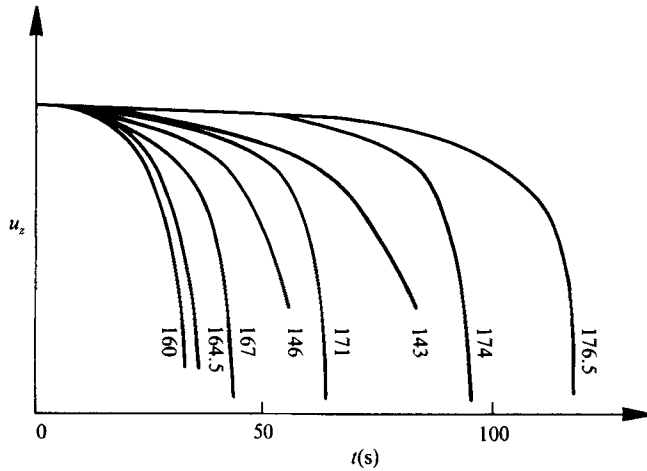


FIGURE 14. Observed relaxation of the axial velocity component versus time of the unstable intermediate states shown in figure 11. Numbers indicate final Reynolds number.

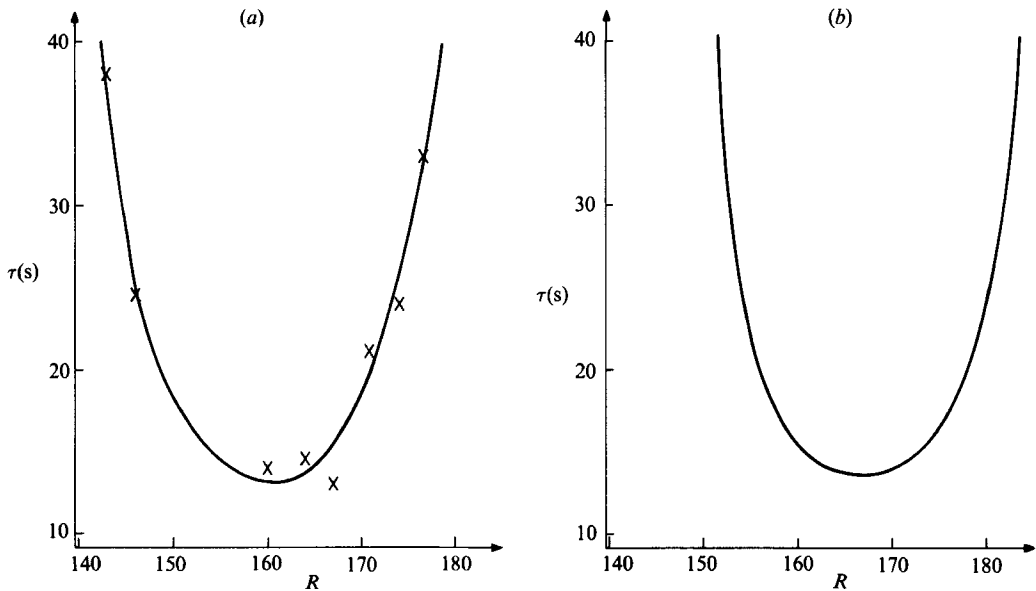


FIGURE 15. Time constants versus Reynolds numbers: (a) experimental points (the line is drawn to guide the eye); (b) calculated.

boundary that separates the basin of attraction of the two nearby stable states. As before the time constant for the relaxation process reaches a maximum value near this boundary and it increases as the bifurcation point is approached. Reasonable quantitative measurements of the time constant could not be made far away from the bifurcation point since the adjustment time of the flow to the new Reynolds number was of the same order as the relaxation time constant. The overall results of the estimated location of the unstable branches are shown in figure 16, where a slight uncoupling due to apparatus imperfections can be seen. In addition, we have included the estimates of the unstable part of the hysteresis region, which was determined as above.

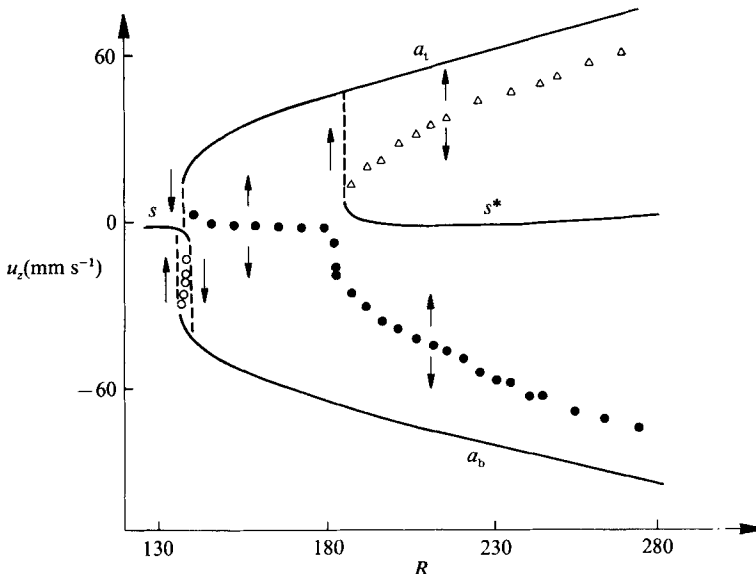


FIGURE 16. Experimentally determined bifurcation diagram showing estimates of the complete branch structure for aspect ratio 1.3. The arrows indicate the relaxation directions, and the points indicate the conjectured unstable branches.

The qualitative agreement between the results obtained here and the solution-branch structure conjectured by Benjamin & Mullin (1981) and numerically confirmed by Cliffe (1983) is very good. This leads us to speculate that there is a connection between our observations of the boundaries of attraction of the stable branches and the unstable branches of the mathematical model. Clearly the dynamics involved could be very complicated but we believe in this case that the very limited number of available solutions gives some substance to our claim.

## 5. Conclusions

The combined experimental and numerical study of this apparently simple form of the Taylor–Couette system has highlighted a variety of complex phenomena. However, the results can be mainly understood in a comparatively straightforward bifurcation model. Estimates for both stable and unstable branches have been presented and on the whole the agreement between experiment and theory is very satisfactory.

A new symmetric state has been observed which has led directly to the uncovering of a period-doubling process. There is qualitative and quantitative agreement between the experimental and numerical results for both the steady and time-dependent forms of this new flow. The bifurcation giving rise to the flow seems to be extremely sensitive to imperfections, and this point warrants further experimental investigation with, perhaps, a greatly enlarged apparatus.

It is perhaps worthy of note that there is preliminary experimental evidence that the steady solution set is still incomplete. A side-by-side two-cell state has been observed at  $R = 2000$ ,  $\Gamma = 0.68$  and investigations are continuing in this regime.

We would like to thank the referees for several useful suggestions. We are indebted to the Stiftung Volkswagenwerk for support of the research programme in the theme

of ‘Synergetik’ and thank Florian Schulz for improving the experimental control. T.M. acknowledges the support of the SERC. The work of K.A.C. was undertaken as part of the Underlying Research Programme of the UKAEA.

#### REFERENCES

- AITTA, A., AHLERS, G. & CANNELL, D. S. 1985 Tri-critical phenomena in rotating Couette–Taylor flow. *Phys. Rev. Lett.* **54**, 673–677.
- BENJAMIN, T. B. 1978*a* Bifurcation phenomena in steady flows of a viscous liquid. I. Theory. *Proc. R. Soc. Lond. A* **359**, 1–26.
- BENJAMIN, T. B. 1978*b* Bifurcation phenomena in steady flows of a viscous liquid. II. Experiments. *Proc. R. Soc. Lond. A* **359**, 27–43.
- BENJAMIN, T. B. & MULLIN, T. 1981 Anomalous modes in the Taylor experiment. *Proc. R. Soc. Lond. A* **377**, 221–249.
- BENJAMIN, T. B. & MULLIN, T. 1982 Notes on the multiplicity of flows in the Taylor experiment. *J. Fluid Mech.* **121**, 219–230.
- BOLSTAD, J. H. & KELLER, H. B. 1987 Computation of the anomalous modes in the Taylor experiment. *J. Comp. Phys.* **69**, 230–251.
- CLIFFE, K. A. 1983 Numerical calculations of two-cell and single-cell Taylor flows. *J. Fluid Mech.* **135**, 219–233.
- CLIFFE, K. A. 1984 Numerical calculations of the primary flow exchange process in the Taylor Problem. *J. Fluid Mech.* (submitted).
- CLIFFE, K. A., JEPSON, A. D. & SPENCE, A. 1986 The numerical solution of bifurcation problems with symmetry with application to the finite Taylor problem. In *Numerical Methods for Fluid Dynamics*, II (ed. K. W. Morton & M. J. Baines), pp. 155–176. Clarendon.
- CLIFFE, K. A. & MULLIN, T. 1985 A numerical and experimental study of anomalous modes in the Taylor problem. *J. Fluid Mech.* **153**, 243–258.
- CLIFFE, K. A. & SPENCE, A. 1985 The calculation of high order singularities in the finite Taylor problem. In *Numerical Methods for Bifurcation Problems* (ed. T. Küpper, H. D. Mittleman & H. Weber), pp. 129–144. Birkhauser.
- CLIFFE, K. A. & SPENCE, A. 1986 Numerical calculations of bifurcations in the finite Taylor problem. In *Numerical Methods for Fluid Dynamics*, II (ed. K. W. Morton & M. J. Baines), pp. 177–207. Clarendon.
- HALL, P. 1982 Centrifugal instabilities of circumferential flows in finite cylinders: the wide gap problem. *Proc. R. Soc. Lond. A* **384**, 359–379.
- HILLE, P. 1984 Realtime measurements of velocity and Reynolds stress in turbulent boundary layers. In *Proc. Second Intl Symp. on Applications of Laser Anemometry to Fluid Mechanics*.
- KELLER, H. B. 1977 Numerical solutions of bifurcation and nonlinear eigenvalue problems. In *Applications of Bifurcation Theory* (ed. P. H. Rabinowitz), pp. 359–384. Academic.
- LÜCKE, M., MIHELICIC, M., WINGERATH, K. & PFISTER, G. 1984 Flow in a small annulus between concentric cylinders. *J. Fluid Mech.* **140**, 343–353.
- MULLIN, T. 1982 Mutations of steady cellular flows in the Taylor experiment. *J. Fluid Mech.* **121**, 207–218.
- MULLIN, T., PFISTER, G. & LORENZEN, A. 1982 New observations on hysteresis effects in Taylor–Couette flow. *Phys. Fluids* **25**, 1134–1136.
- PFISTER, G. 1985 Deterministic chaos in rotational Taylor–Couette flow. In *Flow of Real Fluids* (ed. G. E. A. Meier & F. Obermeier). Lecture Notes in Physics, vol. 235, pp. 199–210. Springer.
- PFISTER, G., GERDTS, U., LORENZEN, A. & SCHÄTZEL, K. 1983 Hardware and software implementation of on-line velocity correlation measurements in oscillatory and turbulent rotational Couette Flow. In *Photon Correlation Techniques in Fluid Mechanics*, pp. 256–263. Springer.
- SCHAEFFER, D. G. 1980 Analysis of a model in the Taylor problem. *Math. Proc. Camb. Phil. Soc.* **87**, 307–337.

- SCHMIDT, H. 1983 Diplomarbeit, University of Kiel, West Germany (unpublished).
- TAYLOR, G. I. 1923 Stability of a viscous liquid contained between two rotating cylinders. *Phil. Trans. R. Soc. Lond. A* **223**, 289–343.
- THOMAS, E. 1979 Sichtbarmachung der Strömung zwischen koaxialen Zylindern: Taylorwirbel und Randeﬀekte. Staatsexamensarbeit, University of Kiel.
- VELTE, W. 1964 Stabilitätsverhalten und Verzweigung stationärer Lösungen der Navier–Stokes-schen Gleichungen. *Arch. Rat. Mech. Anal.* **16**, 97–125.
- VELTE, W. 1966 Stabilität und Verzweigung stationärer Lösungen der Navier–Stokes-schen Gleichungen beim Taylorproblem. *Arch. Rat. Mech. Anal.* **22**, 1–14.